Combustion and Flame 158 (2011) 645–656

Contents lists available at ScienceDirect

Combustion and Flame

journal homepage: www.elsevier.com/locate/combustflame

Combustion kinetic modeling using multispecies time histories in shock-tube oxidation of heptane

David A. Sheen, Hai Wang *

Department of Aerospace and Mechanical Engineering, University of Southern California, Los Angeles, CA 90089, USA

ARTICLE INFO

Article history:
Received 23 September 2010
Received in revised form 14 December 2010
Accepted 14 December 2010
Available online 25 January 2011

Keywords:
Combustion kinetics
Shock tube
Modeling
Uncertainty analysis

ABSTRACT

Recently, species time histories have been measured during *n*-heptane oxidation behind reflected shock waves [D.F. Davidson, Z. Hong, G.L. Pilla, A. Farooq, R.D. Cook, R.K. Hanson, Combust. Flame 157 (2010) 1899–1905]. The highly precise nature of these measurements is expected to impose critical constraints on chemical kinetic models of hydrocarbon combustion. In this paper, we apply the Method of Uncertainty Analysis using Polynomial Chaos Expansions (MUM-PCE) [D.A. Sheen, X. You, H. Wang, T. Løvås, Proc. Combust. Inst. 32 (2009) 535–542] to demonstrate how the multispecies measurement may be utilized beyond simple model validation. The results show that while an as-compiled, prior reaction model of *n*-alkane combustion can be accurate in its prediction of the detailed species profiles, the kinetic parameter uncertainty in the model remains to be too large to obtain a precise prediction of the data. Constraining the prior model against the species time histories within the measurement uncertainties led to notable improvements in the precision of model predictions against the species data as well as the global combustion properties considered. Lastly, we show that while the capability of the multispecies measurement presents a step-change in our precise knowledge of the chemical processes in hydrocarbon combustion, accurate data of global combustion properties are still necessary to predict fuel combustion.

1. Introduction

Recently, highly accurate multispecies time-history data have been made available for shock-tube oxidation of hydrocarbons [1–4]. The species quantified include the parent fuel molecule, C_2H_4, H_2O and CO_2, and radical species, including the CH_3 and OH radicals. The measurements enable us to follow the time sequence of events occurring in a highly-complex reaction process, from initial fuel breakdown, the formation of intermediates, radical build up during and after the induction period, finally to the formation of the combustion products. As a lifelong effort of Professor Hanson culminating advances of laser diagnostics in shock tubes and their applications in combustion reaction kinetics, the multispecies time-history technique has formed the basis for critical testing of chemical reaction models (e.g., [3,4]) and will undoubtedly be valuable to guiding future model development.

An important aspect of this experimental advance is the ultra small uncertainties associated with the measurements. In many cases, they are as small as 5% in the absolute concentration (one–standard deviation). Hence, these multispecies data are expected to contain rich kinetic information that may be utilized beyond their basic usage for model validity. In fact, they impose quantitative constraints on the parameters of a model and its predictions well beyond the condition under which the data are collected. In this paper, we use the Method of Uncertainty Minimization by Polynomial Chaos Expansions (MUM-PCE) [5] to analyze and compare the current uncertainties in our kinetic knowledge against several sets of species time-history data for *n*-heptane oxidation at high temperatures [3,6]. These data are utilized to show how they impact on the accuracy and precision of a reaction model in predicting the global combustion properties, including the laminar flame speed (heat release rate) and ignition delay. Accuracy and precision are used with their conventional statistical meaning, which are, respectively, whether the model prediction agrees with the experiment, and how narrow is the uncertainty in the prediction. We further address the question about the impact of the multispecies time-history data on coupled uncertainties of kinetic rate parameters. Lastly, we demonstrate how the global combustion property measurements may be utilized in conjunction with these data as an inverse problem to obtain a reaction kinetic model that is accurate and precise. *n*-Heptane combustion is used as a test case here not only because it has aroused substantial interests due to its wide use as a model compound to understand the combustion of gasoline and jet fuels, its combustion kinetics is also relatively well understood among liquid hydrocarbon fuels (see, e.g., [7,8]).

* Corresponding author.
E-mail address: haiw@usc.edu (H. Wang).

0010-2180/$ - see front matter © 2011 The Combustion Institute. Published by Elsevier Inc. All rights reserved.
doi:10.1016/j.combustflame.2010.12.016

2. Reaction model

The chemical kinetic model used here is based on JetSurF 1.0 [9], which consists of 196 species and 1462 reactions. JetSurF was developed as a collaborative effort directed at better understanding the combustion chemistry of jet fuels through a surrogate approach. It describes the high-temperature pyrolysis and oxidation of *n*-alkanes up to *n*-dodecane. An earlier version of the model was discussed in You et al. [10]. USC-Mech II [11] was used as the $H_2/CO/C_1$–C_4 kinetic foundation with model details provided in a series of earlier publications [12–23]. The reaction model is largely untuned except for the H_2/CO chemistry, which was based on a comprehensive optimization study conducted earlier [12]. A wide range of validation tests have been conducted and documented online [9,11] or elsewhere [24], considering over 140 sets of global and detailed combustion data. In the current study, the rate parameters of the H_2/CO subset were restored to their nominal, as-compiled values. Additionally, the rate parameter for the $OH + HO_2 \leftrightarrow H_2O + O_2$ reaction was revised using the expression of Baulch et al. [25] in light of the recent work of Hanson, Michael and co-workers [26,27]. Extrapolating their kinetic rates show little evidence of a peculiar drop in the rate coefficient near 1000 K as reported in [28,29].

The reaction model described above is referred to as the unconstrained model, or Model I, since all rate coefficients were taken as they are from the literature. Uncertainty factors for Arrhenius pre-factors in the $H_2/CO/C_1$–C_4 subset (i.e., USC-Mech II) are given in the supplemental materials of [5]. These factors were taken in consultation with literature compilations (e.g., [25,30]) or from our own evaluations. The pre-factors for all reactions not considered in USC-Mech II are assumed to have an uncertainty factor of 3. The uncertainty in the activation energy or the pressure fall-off parameters is not considered in the present work. Such uncertainties inevitably exist in reaction models currently available, and in many cases, their impact on the overall uncertainty of the model and its predictions can be rather large. This nonlinear uncertainty effect will be considered in a future work.

3. Experimental datasets

The data considered here are two sets of C_2H_4, OH, H_2O and CO_2 time histories (Series 1*i* and 1*ii*) [3] and three CH_3 time histories (Series 2*i*–*iii*) [6], all of which were determined for stoichiometric shock-tube oxidation of highly diluted *n*-heptane in oxygen and argon. The experimental conditions are summarized in Table 1. Additionally, two types of global combustion properties of *n*-heptanes were considered, ignition delay times and laminar flame speeds. They provide useful information concerning the impact of multi-species time histories on the model predictions of global combustion responses. Series 3 contains five sets of ignition delay data for three *n*-heptane–oxygen–argon mixtures [31,32], spanning the equivalence ratio range of 0.5–2.0 and pressures from 1 to 4 atm. Series 4 is a set of laminar flame speed data at the atmospheric pressure [24]. Uncertainty in the ignition delay time is estimated at ±20% based on a regression of the data. Laminar flame speed uncertainty is estimated at ±2 cm/s. Again the conditions of the last two series of experiments are listed in Table 1.

It should be noted that the model posterior uncertainty space depends strongly on the uncertainties of the experimental measurements. In [3], the measurement uncertainty in [OH] is ±3%, but the precision of the measurement is confounded somewhat by the uncertainty in the post-shock temperature T_5. To illustrate this point, we show in Figs. 1 and 2 the nominal predictions of the OH, H_2O, CO_2, and C_2H_4 profiles using Model I for Series 1*i* and 1*ii* experiment, respectively. The solid lines designate calculations at the nominal temperature of the experiments; the long-dashed lines represent those calculated with ±10 K uncertainty (2σ-standard deviation) in T_5. It can be seen that in regions of large gradients the species measured can be influenced to a greater extent by the uncertainty of the temperature than in the concentration itself. We present, for comparison, a uniform uncertainty of ±20% in the predicted species profiles, as shown by the short-dashed lines in both figures, which is similar in magnitude to the propagated uncertainty from T_5. Even if the species concentration could be measured exactly, the inherent uncertainty in T_5 dictates the uncertainties of the measurement. In light of this result, we

Table 1
Experimental datasets considered.

Series	Data type/conditions[a]	Model constraints				
		I	II	III	IV	V
1	OH, CO_2, H_2O, C_2H_4 time histories [3] (i) 300 ppm nC_7H_{16}/3300 ppm O_2/Ar[b] T_5 = 1494 K, p_5 = 2.15 atm (ii) 300 ppm nC_7H_{16}/3300 ppm O_2/Ar[c] T_5 = 1365 K, p_5 = 2.35 atm		×	×		×
2	CH_3 time histories [6] 500 ppm nC_7H_{16}/5500 ppm O_2/Ar (i) T_5 = 1395 K, p_5 = 1.72 atm (ii) T_5 = 1461 K, p_5 = 1.67 atm (iii) T_5 = 1545 K, p_5 = 1.61 atm			×		×
3	Ignition delay (i) 0.4% nC_7H_{16}/4.4% O_2/Ar (a) T_5 = 1429–1486 K, p_5 = 1 atm [31,32] (b) T_5 = 1383–1503 K, p_5 = 2 atm [31,32] (c) T_5 = 1394–1474 K, p_5 = 4 atm [32] (ii) 0.4% nC_7H_{16}/2.2% O_2/Ar T_5 = 1499–1700 K, p_5 = 1 atm [31,32] (iii) 0.4% nC_7H_{16}/8.8% O_2/Ar T_5 = 1300–1499 K, p_5 = 1 atm [31,32]				×	×
4	Laminar flame speeds (nC_7H_{16}/air) [24] T_u = 353 K, p = 1 atm				×	×

[a] The uncertainty of T_5 in Series 1 and 2 is ±10 K ($2-\sigma$ deviation).
[b] Actual T_5 and p_5 values: 1494 K, 2.155 atm (OH and CO_2), 1502 K, 2.262 atm (H_2O), 1506 K, 2.36 atm (C_2H_4).
[c] Actual T_5 and p_5 values: 1378 K, 2.326 atm (OH), 1375 K, 2.282 atm (CO_2), 1368 K, 2.86 atm (H_2O), 1358 K, 2.436 atm (C_2H_4).

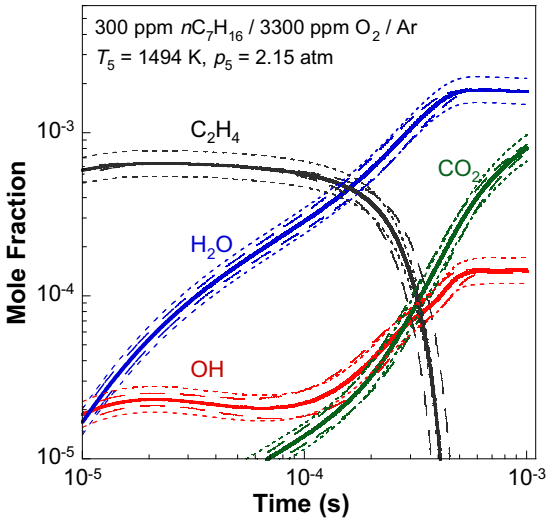

Fig. 1. Uncertainty estimates for species time history measurements (Series 1*i* of Table 1). Solid line: predictions of reaction Model I at the nominal temperature shown; long-dashed lines: computed uncertainty bounds due to ±10 K uncertainty in the T_5 value [3]; short-dashed lines: 20% uncertainty on the nominal mole fraction values.

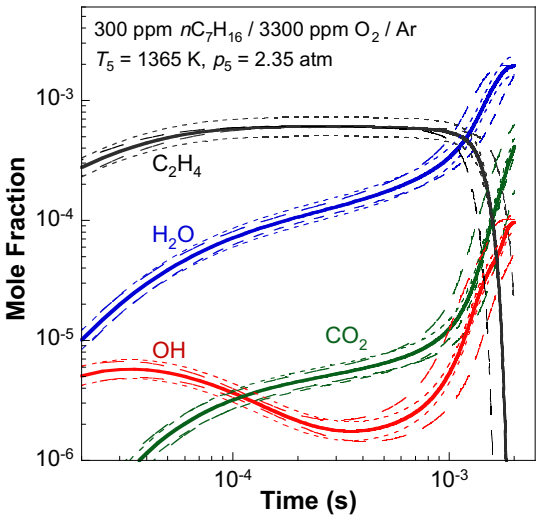

Fig. 2. Uncertainty estimates for species time history measurements (Series 1*ii* of Table 1). Solid line: predictions of reaction Model I at the nominal temperature shown; long-dashed lines: computed uncertainty bounds due to ±10 K uncertainty in the T_5 value [3]; short-dashed lines: 20% uncertainty on the nominal mole fraction values.

assigned a uniform uncertainty of ±20% for Series 1*i* over the entire time period considered and for Series 1*ii* during the induction period prior to 800 μs. For the lower temperature measurements after 800 μs (Series 1*ii*: T_5 = 1365 K), the T_5 uncertainty has a much greater impact on the species predictions, close to a factor of 3. We therefore assign an uncertainty factor of 3 to the Series 1ii measurements at 1000 μs.

As stated in Ref. [6], the uncertainty in the CH_3 concentration is ±20%. Simulation shows that the ±10 K uncertainty in T_5 impacts the concentrations of CH_3 only in the later part of the reaction leading to its complete destruction (Fig. 3). Hence, we assigned all CH_3 profiles a uniform uncertainty of ±20%.

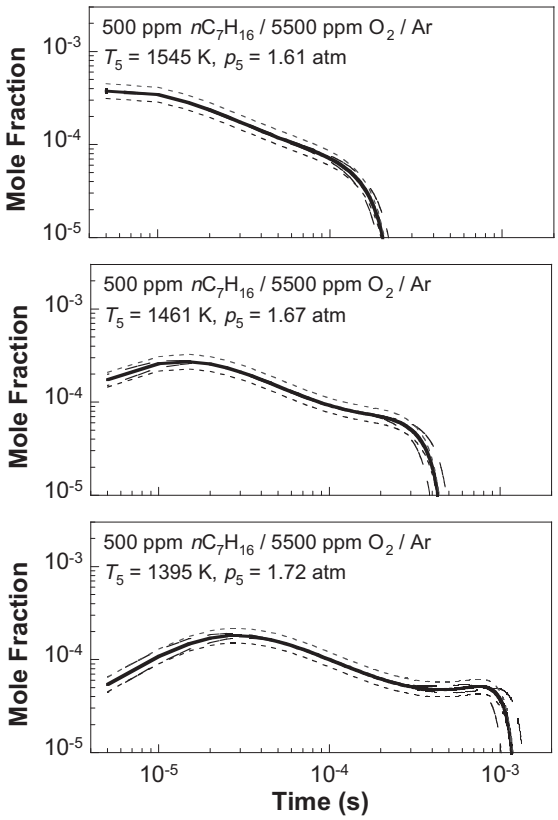

Fig. 3. Uncertainty estimates for CH_3 time history measurements (Series 2 of Table 1). Solid line: predictions of reaction Model I at the nominal temperature shown; long-dashed lines: computed uncertainty bounds due to ±10 K uncertainty (2σ standard deviation) in the T_5 value [3]; short-dashed lines: 20% uncertainty on the nominal mole fraction values.

4. The method of uncertainty minimization by polynomial chaos expansions (MUM-PCE)

Uncertainty quantification in chemical reaction models is much younger than the numerical study of combustion flows. A rudimentary methodology for propagating the reaction rate uncertainty into a prediction, using localized sensitivity analysis, was first proposed by Warnatz [33]. Turanyi and co-workers expanded this method [34] and later combined it with a Monte Carlo approach [35–38] to estimate the parametric uncertainty in laminar flame-speed predictions of the Leeds hydrocarbon oxidation model [39]. Tomlin and co-workers, likewise, have applied high-dimensional model representation (HDMR) [40] to the problem of uncertainty analysis. Uncertainty quantification of constrained models is somewhat newer; the only work in this area has been that of Beck et al. [41–44] in the context of structural engineering, as well as the work of Frenklach and co-workers [45–47] and our own Method of Uncertainty Minimization using Polynomial Chaos Expansions (MUM-PCE) [5,48].

MUM-PCE combines multiparameter minimization through solution mapping [49,50] with the spectral uncertainty method [51,52], as introduced by Najm and co-workers [53–55]. The method was developed as a means of propagating the uncertainties in the rate parameters of a model in its prediction of a combustion property. The method is capable of constraining the model uncertainties with a set of experimental measurements of combustion phenomena with well characterized uncertainty. In this method, each Arrhenius pre-factor is normalized as a factorial variable $x_k = \ln(A_k/A_{k,0})/\ln f_k$ [49,50], where A_k is the Arrhenius pre-factor of the kth reaction, $A_{k,0}$ is its nominal value, and f_k is the uncertainty factor of the rate coefficient. Uncertainty analysis in MUM-PCE expresses the factorial variables as polynomials of some basis random variable vector ξ,

$$\mathbf{x} = \mathbf{x}_0 + \sum_{i=1}^{M} \boldsymbol{\alpha}_i \xi_i + \sum_{i=1}^{M} \sum_{j=i}^{M} \boldsymbol{\beta}_{ij} \xi_i \xi_j + \ldots, \tag{1}$$

where $\mathbf{x}$ is the generalized vector of rate parameters, $\boldsymbol{\alpha}$ and $\boldsymbol{\beta}$ are coefficients, and M is the number of variables considered. Including only first-order terms in Eq. (1) gives a normally distributed $\mathbf{x}$, assuming ξ's are themselves normally distributed. Adding higher-order terms allows $\mathbf{x}$ to take on higher-order moments, although these will not be considered here. This expression is the stochastic expression for the factorial variable vector, and the coefficients include within it the entire uncertainty expression for $\mathbf{x}$.

In the absence of any further information, as is usually the case for an as-compiled model, the factorial variables can be assumed to be normally distributed and independent, which is equivalent to letting $x_i = 1/2\xi_i$. This means that each reaction rate parameter is log-normally distributed with a 2σ uncertainty factor equal to f_i. It should be noted that assigning such a distribution requires assuming that all rate constants have been measured statistically meaningful number of times, but this is untrue for almost all reactions considered, including the $H + O_2 = O + OH$ reaction. This limitation turns out to be inconsequential to the final results. A result study [48] shows that assuming the rate parameters to be

uniformly distributed within f_i leads to essentially the same result as a log-normal distribution.

Within this framework, $x_i = -1$ and $+1$ represents the lower and upper bounds of the natural logarithm of the rate coefficient. The prediction uncertainty of a model may be assessed by a Monte Carlo procedure wherein numerical computations are carried out over a large set of $\mathbf{x}$ sampled over a normal distribution of $\sigma_i = 1/2$. Because simulations of shock-tube experiments are usually not time consuming, prediction uncertainties are calculated numerically by solving the underlying initial value problems for the set of $\mathbf{x}$ sampled.

For flame simulations, however, direct Monte Carlo sampling is computationally expensive. MUM-PCE uses the method of solution mapping [49,50,56] and assumes that the dependence of a model prediction η_r may be mapped with respect to the factorial variables by, for example, a second-order polynomial [57],

$$\eta_r(\mathbf{x}) = \eta_{r,0} + \sum_{i=1}^{N_r} a_i x_i + \sum_{i=1}^{N_r} \sum_{j \geq i}^{N_r} b_{ij} x_i x_j, \tag{2}$$

where $\eta_{r,0}$ is the nominal prediction of the base model for the rth experiment and N_r is the number of active rate parameters. As a general rule, N_r represents the number of active parameters and is typically of the order of 10 for any particular experiment. The active parameters can be determined by a one-at-a-time sensitivity analysis [33], or by methods such as HDMR [40]. The response surface coefficients a_i and b_{ij} are generated either by using a sensitivity-analysis-based design (SAB) [56] or by a central-composite factorial design [57] if sensitivity information is unavailable.

The stochastic expression (2) is inserted into the response surface Eq. (1), generating a stochastic expression for each η_r,

$$\eta_r(\xi) = \eta_r(\mathbf{x}_0) + \sum_{i=1}^{M} \hat{\alpha}_{r,i} \xi_i + \sum_{i=1}^{M} \sum_{j=i}^{M} \hat{\beta}_{r,ij} \xi_i \xi_j + \ldots, \tag{3}$$

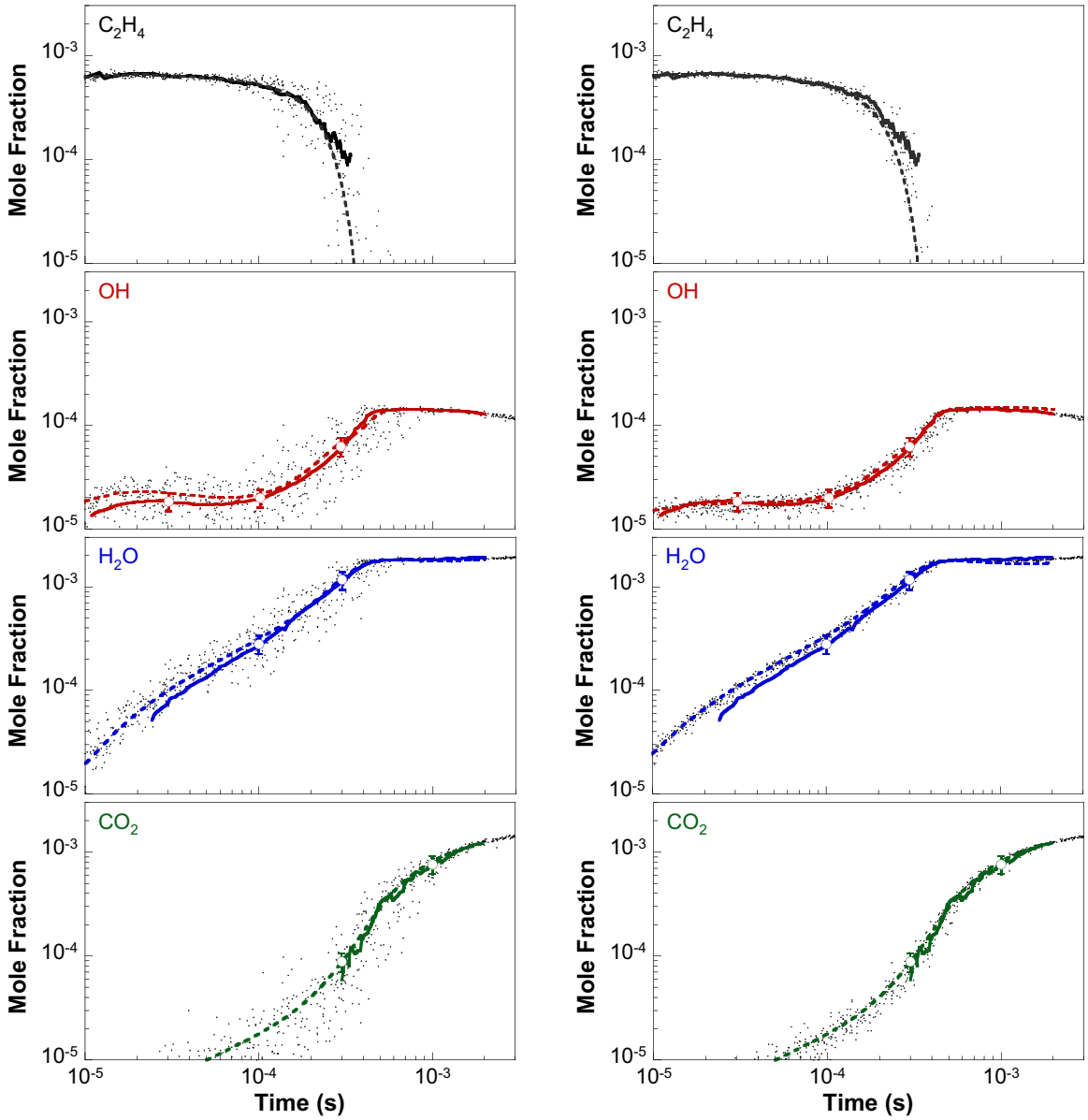

Fig. 4. Experimental (solid lines [3]) and computed (dashed lines: nominal prediction; dots: uncertainty scatter) species time histories for Series 1*i*: 300 ppm nC_7H_{16}/3300 ppm O_2/Ar, $T_5 = 1495$ K, $p_5 = 2.15$ atm (see Table 1). The open circles and the corresponding error bars designate data used as Series 1 targets and 2σ standard deviations, respectively. Left panel: prior model (Model I). Right panel: posterior model (Model II).

which has variance equal to

$$\sigma_r^2(\mathbf{x}) = E[\eta_r^2(\xi)] - E^2[\eta_r(\xi)] = \sum_{i=1}^{M} \hat{\alpha}_{r,i}^2 + 2\sum_{i=1}^{M} \hat{\beta}_{r,ii}^2 + \sum_{i=1}^{M-1}\sum_{j=i+1}^{M} \hat{\beta}_{r,ij}^2, \quad (4)$$

where $E[]$ is the expectation operator. Hence, in the framework of MUM-PCE, the predictions of a kinetic model consist of the nominal prediction $\eta_r(\mathbf{x}_0)$ and its standard deviation σ_r.

High-quality experiments, like those reported in [3, 6], provide constraints on the model accuracy and precision, both of which may be quantified through multiparameter optimization. In such an optimization, a set of experiments are chosen to form the optimization target set. Each target has an observed value η_r^{obs} along with its uncertainty σ_r^{obs}. An optimized $\mathbf{x}_0^*$ set, representing the constrained model, is obtained by minimizing the least-squares difference between the model predictions and the experimental measurements, weighted by the experimental uncertainty, i.e.,

$$\Phi(\mathbf{x}_0^*) = \min_{\mathbf{x}} \left(\sum_{r=1}^{n} \left\{ \frac{[\eta_r(\mathbf{x}) - \eta_r^{\text{obs}}]}{\sigma_r^{\text{obs}}} \right\}^2 + \sum_{k=1}^{N} 2x_k^2 \right). \quad (5)$$

The first term is the least-squares difference between the targets and model predictions, and the second term comes from treating each rate parameter value as an experiment in its own right. The uncertainty in the constrained model can be estimated by a multivariate normal distribution [48]

$$\mathbf{x}^* = \mathbf{x}_0^* + \sum_{i=1}^{M} \boldsymbol{\alpha}_i^* \xi_i. \quad (6)$$

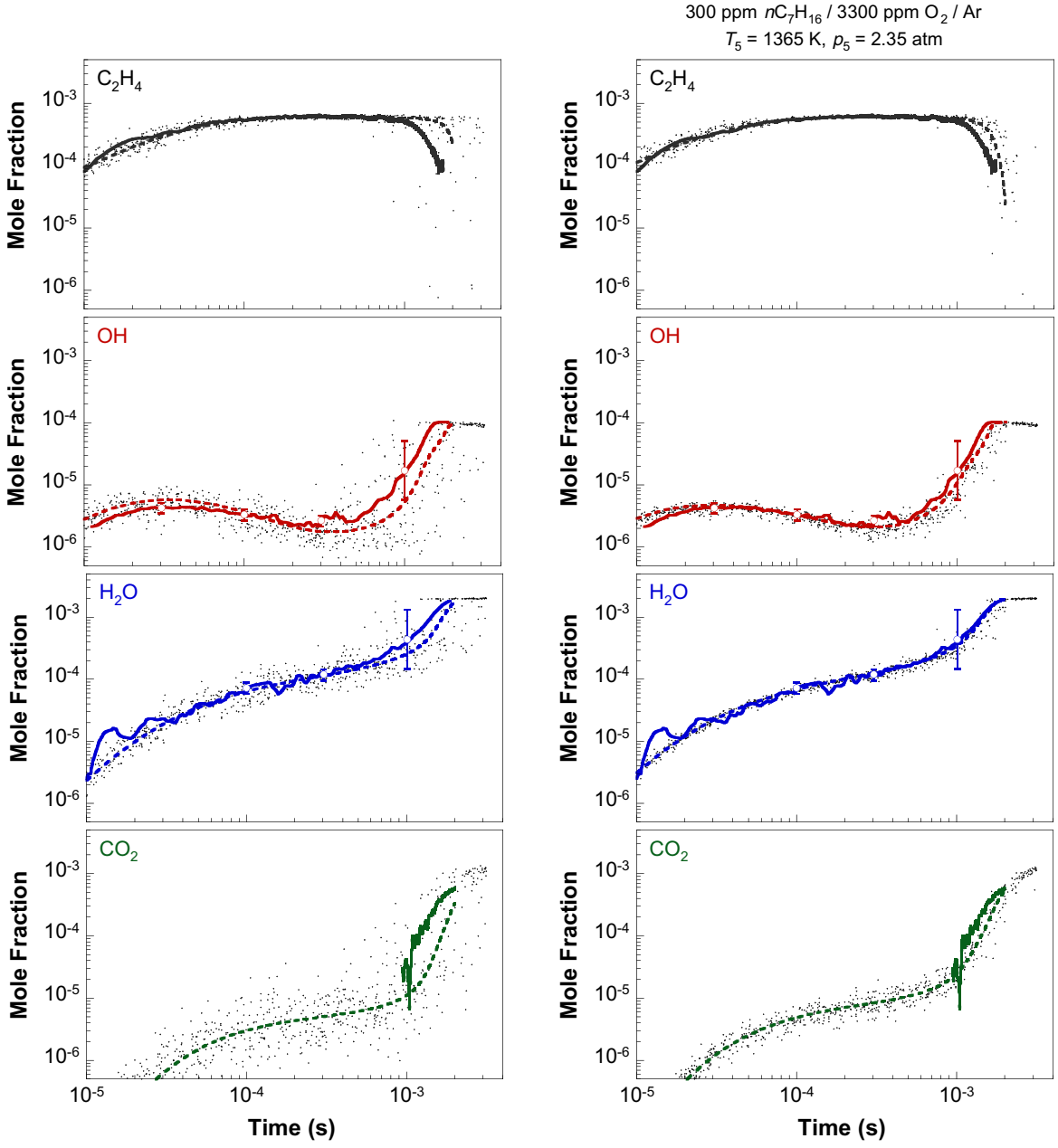

Fig. 5. Experimental (solid lines [3]) and computed (dashed lines: nominal prediction; dots: uncertainty scatter) species time histories for Series 1*ii*: 300 ppm nC_7H_{16}/3300 ppm O_2/Ar, T_5 = 1365 K, p_5 = 2.35 atm (see Table 1). The open circles and the corresponding error bars designate data used as Series 1 targets and 2σ standard deviations, respectively. Left panel: prior model (Model I). Right panel: posterior model (Model II).

with mean $\mathbf{x}_0^*$ and covariance matrix $\Sigma = \boldsymbol{\alpha}^{*T}\boldsymbol{\alpha}^*$. We find $\boldsymbol{\alpha}^*$ by linearizing the response surfaces (Eq. (2)) in the neighborhood of $\mathbf{x}_0^*$, which gives $\eta_r \cong (\mathbf{x}_0^{*T}\mathbf{b}_r + \mathbf{a}_r)\mathbf{x}$. Then, Σ is given by

$$\Sigma \cong \left[\sum_{r=1}^{N} \frac{\mathbf{W}_r(\mathbf{x}_0^*)}{\left(\sigma_r^{\text{obs}}\right)^2} + 2\mathbf{I}\right]^{-1}, \tag{7}$$

where $\mathbf{W}_r(\mathbf{x}) = \mathbf{b}_r\mathbf{x}\mathbf{x}^T\mathbf{b}_r + \mathbf{a}_r\mathbf{x}^T\mathbf{b}_r + \mathbf{b}_r^T\mathbf{x}\mathbf{a}_r^T + \mathbf{a}\mathbf{a}_r^T$ and $\mathbf{I}$ is the identity matrix.

The constrained model $\mathbf{x}_0^*$ and associated parameter uncertainty $\boldsymbol{\alpha}^*$ obtained by solving Eqs. (5) and (7) represent the best possible fit to the experimental measurements and uncertainties, given the *a priori* selection of rate parameters and uncertainty bounds that went into the as-compiled model. It is possible, however, that the predictions of the initially constrained model will fall out of the target uncertainty bounds. This happens if either an experimental measurement or a rate evaluation is incorrect, or if the uncertainty of either is underestimated. To that end, we include a method of flagging and removing experiments that are inconsistent with other data and the final model. Of course, the cause for the disagreement can also be caused by incompleteness of a model. Thus a rejected set of data do not directly infer the data to be inaccurate. Rather, it suggests that if such data can be reproduced experimentally, the validity of the unconstrained model will require scrutiny.

After Eq. (5) has been solved, targets are checked for inconsistency by calculating the contribution of the rth experiment to the objective function,

$$F_r = \frac{\eta_r^{\text{obs}} - \eta_r(\mathbf{x}_0^*)}{2\sigma_r^{\text{obs}}}. \tag{8}$$

The rth experiment is flagged as inconsistent with the model and removed from the target set if this target is the only one with $F_r > 1$. When multiple targets have $F_r > 1$, it is possible that removing inconsistent target would lead to an entirely consistent model with all F_r's < 1. So the consistency algorithm will only ever remove one target at a time, and this target has the largest weighted scalar product D_rF_r, where D_r is

$$D_r = \frac{\nabla\eta_r(\mathbf{x}^*)\cdot\mathbf{x}^*}{\|\nabla\eta_r(\mathbf{x}^*)\|\|\mathbf{x}^*\|}. \tag{9}$$

Then Eq. (5) is solved again until all targets have $F_r \leqslant 1$.

5. Computational details

The shock tube problem was solved using the Sandia ChemKin code [58] with a constant density model for both species time histories and ignition delay times. All ignition delay data considered here were measured by the onset of OH* emission. Computationally, the ignition point was determined from the maximum $d[\text{OH}^*]/dt$. Because the underlying problem is neither constant density nor constant pressure, the current approximation is expected to yield reasonably good comparison between model and experiment. Premixed flame simulations were performed using Sandia Premix [59], with multicomponent transport, with updates taken from [60,61].

Active parameters for each experiment were determined using one-at-a-time sensitivity analysis and are listed in Table S1 of the supplementary material. Parameters were screened by ranking the reaction pre-factors in order of their uncertainty-weighted sensitivity coefficients, defined as $S_{w,ik} = S_{ik} \ln f_k$ where S_{ik} is the sensitivity coefficient of the ith experiment to the kth rate parameter, and choosing those for which $S_{w,ik}$ was less than 10% of the largest for any given experiment. This procedure was chosen because $S_{w,ik}$ is a measure of the uncertainty contribution of each reaction to that particular experiment. Response surfaces for laminar flame speeds and species profiles were determined using the SAB method [56], while those for ignition delay times were determined using a central-composite fractional factorial design of resolution VI [57]. Minimization of the objective function used the constrained-optimization ZXMWD subroutine of the International Math Subroutine Library. Calculation of $\boldsymbol{\alpha}^*$ used the SLATEC Common Mathematical Library.

As we discussed earlier, the untuned, base model is termed Model I. To examine the impact of the Stanford multispecies time-history data on model accuracy and precision, we constrained the base model by the Series 1 data [3] only, yielding Model II. Next, we consider both Series 1 and 2 data, yielding Model III. To compare the impact of multispecies time-history data and that of global combustion properties (ignition delay and laminar flame speeds), we constrained the base model for data in Series 3 and 4 only. This produced Model IV. Lastly, we considered both multispecies time-history data and the combustion properties, which yielded a fully constrained, Model V. In Bayesian terminology, Model I is the "prior" model since it denotes the state of knowledge before any global experiments are taken into account [62]. All the other models are therefore "posterior" models. A summary of the

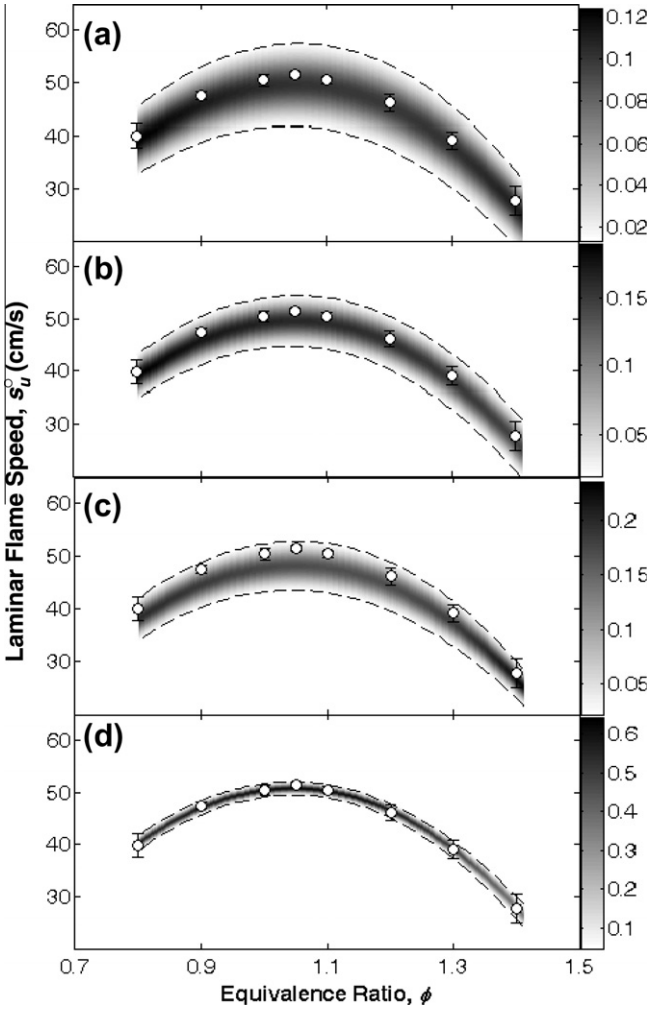

Fig. 6. Probability density function of laminar flame speed predicted for heptane–air mixtures (p = 1 atm, T_u = 353 K). The pair of dashed lines bracket the 2σ standard deviation. Panel (a) prior model (Model I in Table 1); (b) posterior model (Model II using Series 1 data), (c) posterior model constrained by Series 1 data with a uniform uncertainty value of ± 5%, (d) posterior model constrained by all data of Table 1. Symbols are experimental data taken from Ref. [24].

posterior models is presented in Table 1 and the rate parameters of these models are presented in Table S3 of the supplementary material.

6. Results and discussion

To illustrate the utility of the multispecies time-history data, we plot in Figs. 4 and 5 comparisons of measured and computed profiles for Series 1 experiments. The dashed lines and scattered dots represent nominal predictions and the results of Monte Carlo sampling of model uncertainties for the prior model (Models I, left panels) and posterior model (Model II, right panels). As it is seen, the nominal prediction of the prior model is in good agreement with the data, but the precision of the model prediction is poor. For example, while the nominal prediction for the OH mole fraction falls within the uncertainty of the experiment over a wide range of reaction times, the uncertainty of the model prediction is at least a factor of 2, as judged by the width of the scatter before the OH model fraction reaches the plateau region where chemical equilibrium governs. Hence, the results shown in the left panels of Figs. 4 and 5 illustrate the fact that the prior model is accurate but not always precise. The fact that the model uncertainty is larger than the equivalent experiment shows that these data will be useful to constrain the uncertainty of the prior model.

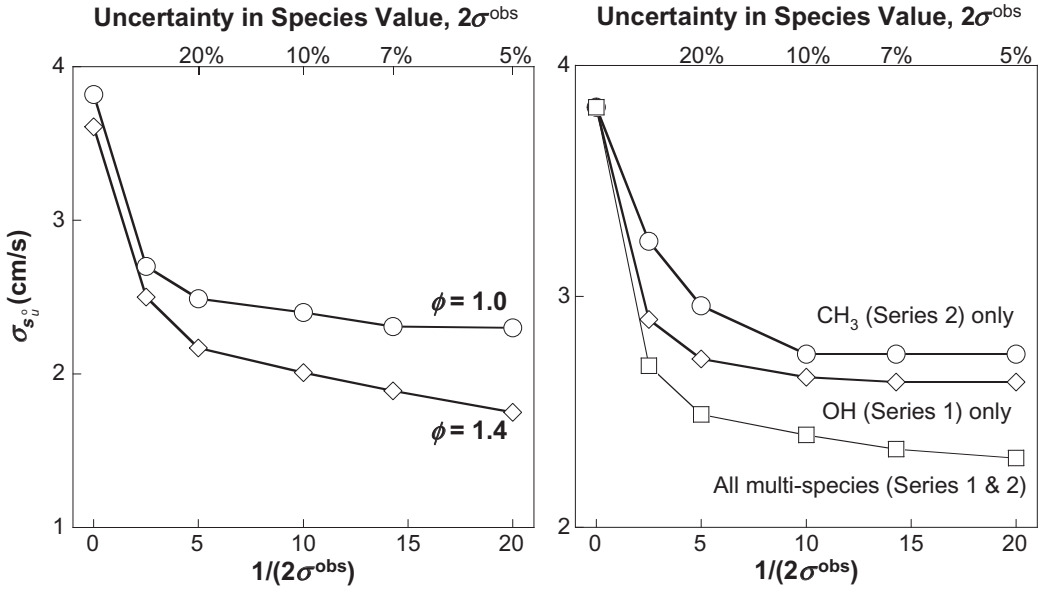

Fig. 7. Variation of the standard deviation predicted for the heptane–air laminar flame speed (T_u = 353 K, p = 1 atm) as a function of the percentage uncertainty in the species time-history data. Left panel: prior and posterior models constrained with Series 1 data; right panel: impact of species time histories selected on posterior model.

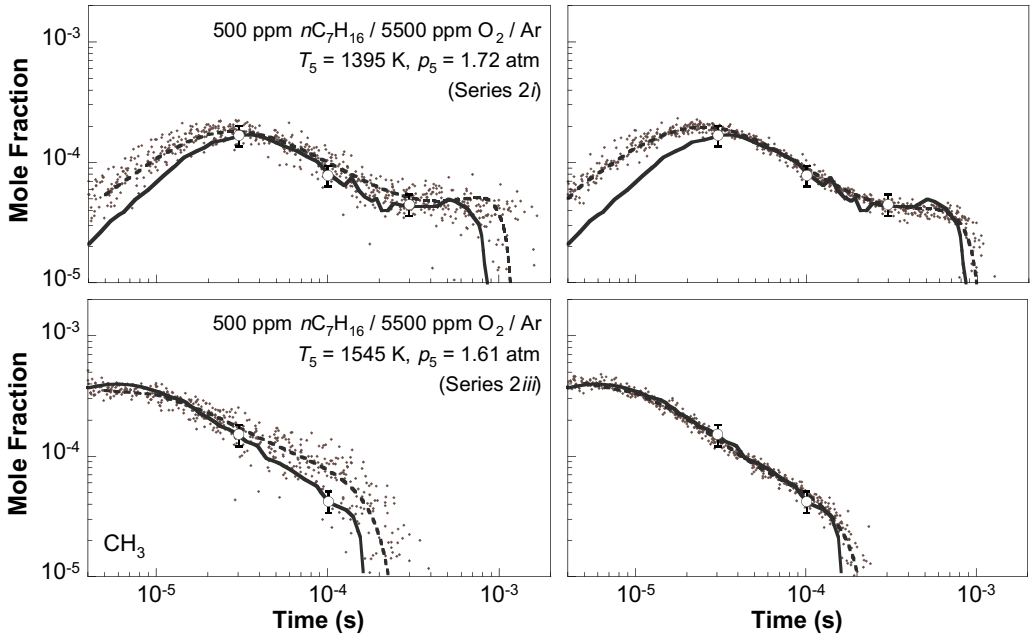

Fig. 8. Experimental (solid lines [6]) and computed (dashed lines: nominal predictions; dots: uncertainty scatter) CH_3 time histories of Series 2*i* and 2*iii* (see Table 1). The open circles and the corresponding error bars designate data used as Series 2 targets and 2σ standard deviations, respectively. Left panel: prior model (Model I). Right panel: posterior model (Model III).

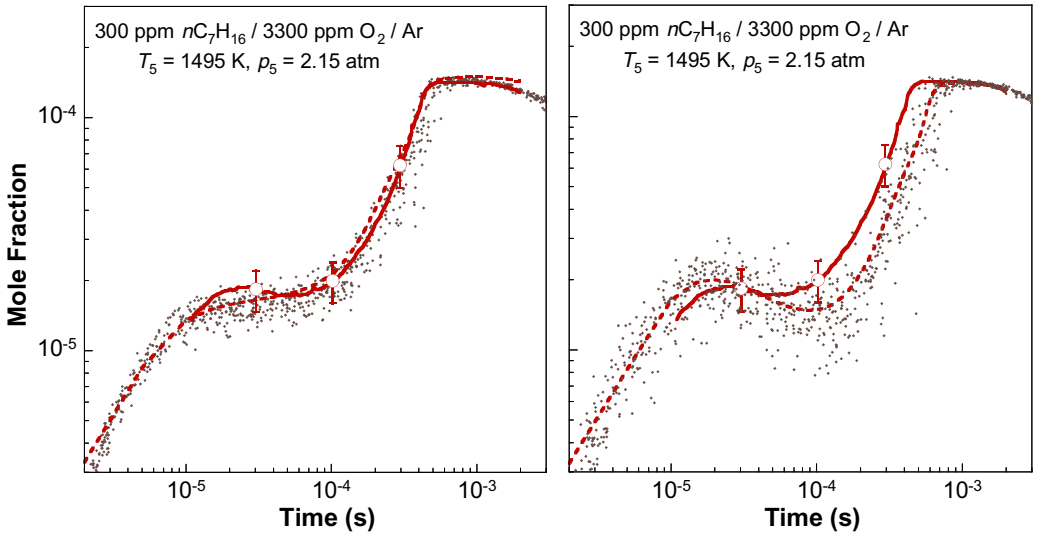

Fig. 9. Experimental (solid lines [3]) and computed (dashed lines: nominal predictions; dots: uncertainty scatter) OH time history of Series 1*i* (see Table 1). The open circles and the corresponding error bars designate data of Series 1 targets and 2σ standard deviations, respectively. Left panel: posterior model constrained by Series 1 and 2 time histories (Model III). Right panel: posterior model constrained against laminar flame speeds and ignition delay times (Model IV).

Indeed, after Model I is constrained using just a few data points (marked by the open symbols in Figs. 4 and 5), we observed not only a significantly narrowed uncertainty band in the predictions, but an even better agreement between the data and nominal prediction for these species profiles, as exhibited on the right panels of both Figs. 4 and 5. The impact of these multispecies time-history data on the model precision is depicted in Fig. 6. The top plot (a) shows the probability density function and the 2σ standard deviation of laminar flame speeds of *n*-heptane–air mixtures predicted by the prior model. Again, the results may be best described as, the nominal prediction by the model is accurate, but the precision is rather poor. In particular, the 2σ standard deviation can be larger

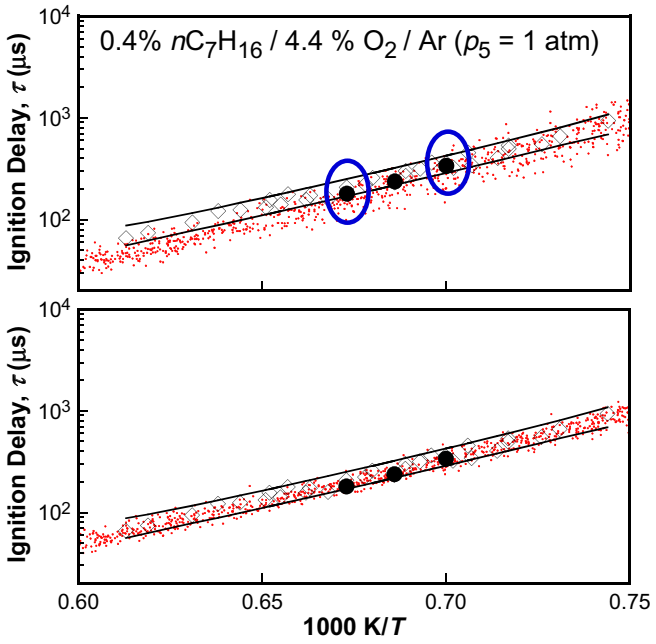

Fig. 10. Ignition delay times of Series 3*ia*. Experiments: ◇, [32]; ●, [31]. Dots represent the results of Monte Carlo sampling of predictions by Model II (top panel) and Model V (bottom panel). The circled data indicate the temperatures of the ignition delay targets.

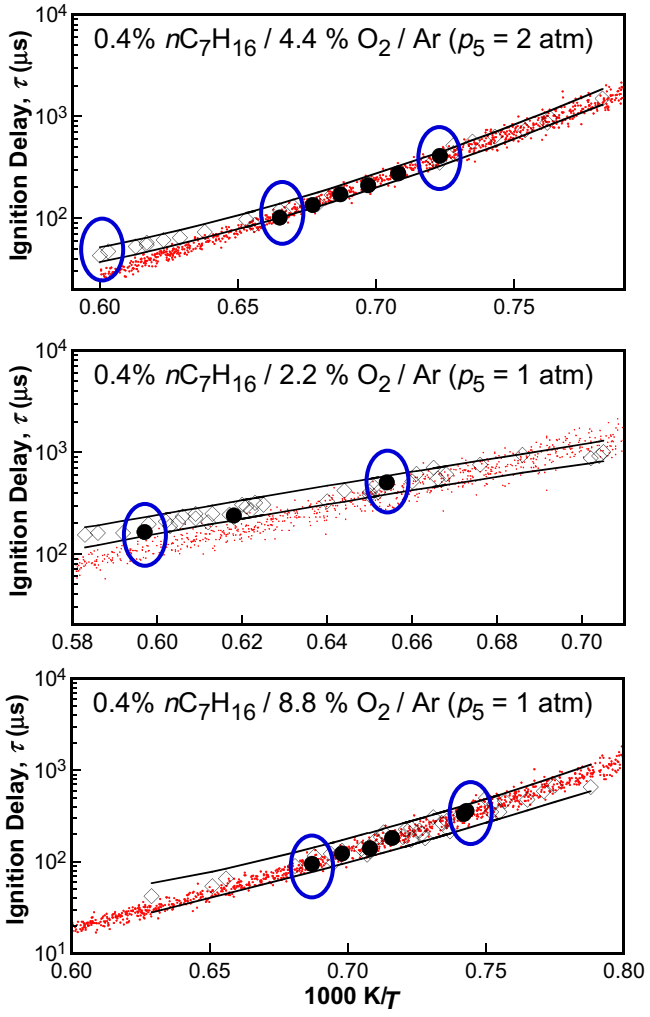

Fig. 11. Ignition delay times for Series 3*ib* (top panel), Series 3*ii* (middle panel) and Series 3*iii* (bottom panel). Experiments: ◇, [32]; ●, [31]. Dots represent the results of Monte Carlo sampling of predictions by Model V. The circled data indicate the temperatures of the ignition delay targets.

than 10 cm/s for a flame speed value of 50 cm/s. In panel (b), we present the results of Model II. The two sets of species data along reduce the uncertainty of the predicted flame speeds by almost a factor of 2. Clearly this result illustrates that the value of the multispecies measurement is well beyond the usage of model validation.

We digress here to discuss the impact of the accuracy of the species measurement on laminar flame-speed predictions. In the left panel of Fig. 7, we show the standard deviation of predicted flame speeds at two equivalence ratios (ϕ = 1.0 and 1.4) as a function of the hypothetical experimental uncertainties in the species measurement. The $1/(2\sigma^{obs})$ value of 0 represents the prior knowledge in which Series 1 data do not exist. As seen, while the current data with ±20% uncertainty lowers the model uncertainty notably, further improved accuracies in the data does not appear to offer significant benefits. The analysis here also shows that an even more careful uncertainty analysis is critical to the utilization of highly precise data. For example, if a ±5% uncertainty is assigned to all species concentration (i.e., neglecting the uncertainty due to T_5), the model can become ill-constrained. Panel (c) of Fig. 6 shows that the nominal flame-speed prediction becomes notably lower than the experimental data, when a ±5% uncertainty is assigned to all species concentration.

The prior model can also be constrained by the CH_3 profiles published earlier [6] (Series 2 experiments). As examples, we show in Fig. 8 the comparison of experimental data of two such profiles and the predictions of both the prior model and Model III. Again the prior model considered here is accurate but not precise (the left panels of Fig. 8), but it can be constrained by the measurements leading to a notably precise model (the right panels). Here we considered only the data (marked by the open symbols) beyond the first peaks in the CH_3 profiles. In general, the peak methyl concentration is reached around or before 10 μs reaction time. Notable disagreement exists between the measurement and both the prior

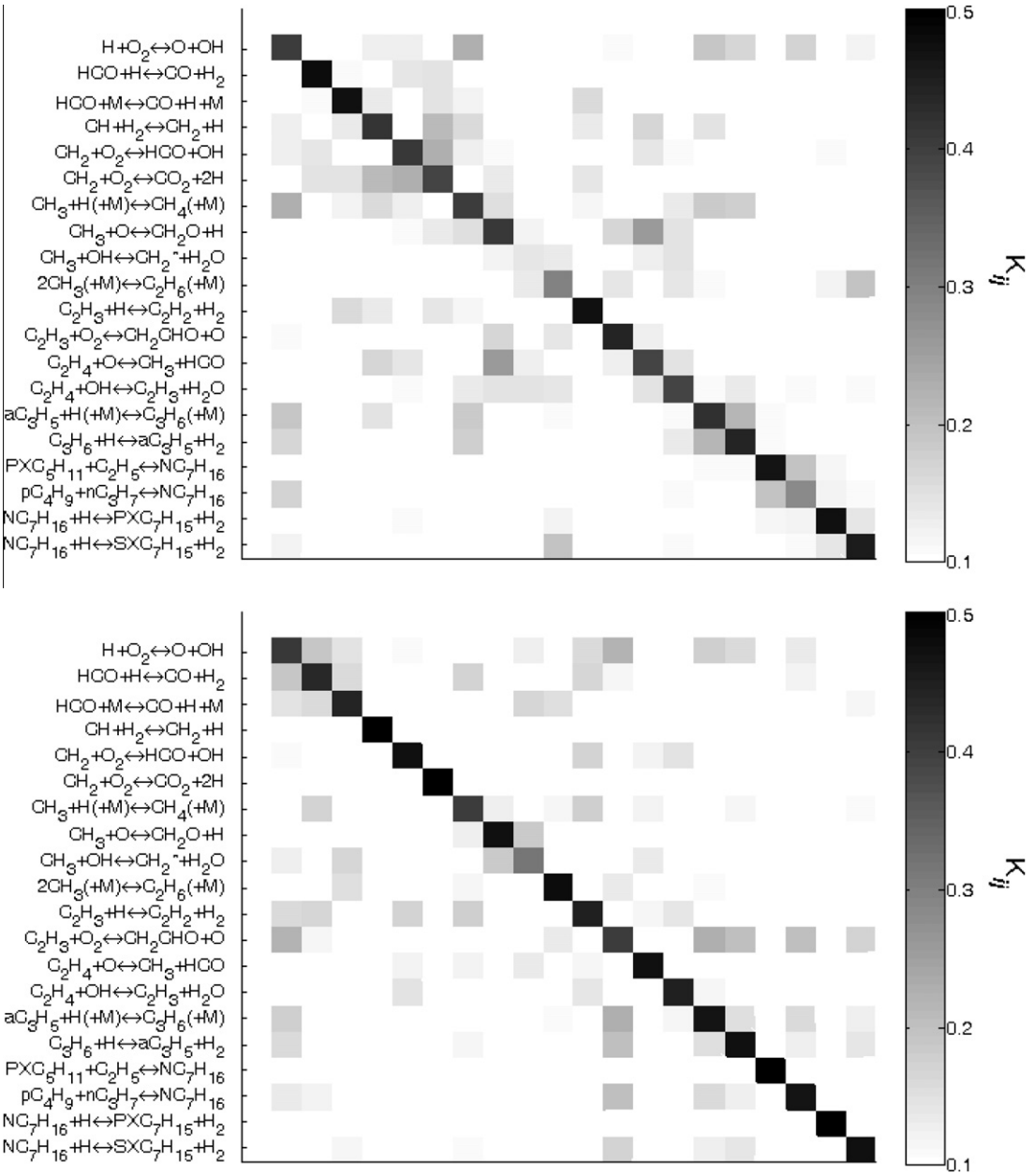

Fig. 12. Covariance matrices computed for Models II (top panel) and Model IV (bottom panel), presented as $K_{ij} = \sqrt{|\Sigma_{ij}|}$.

and posterior models for Series 2*i*. Attempts to include the data prior to CH_3 peaking yielded inconsistency among datasets considered for the prior model used. Hence, the results, especially that shown in the upper-right panel of Fig. 8 suggest that either the reaction model misses critical reactions important to the very early stage of the fuel break down or it is unable to capture the mixture condition within the first few microseconds of reflected shock passage. This problem will be examined in a future work.

Regardless, the methyl time histories have similar impact on the precision of the flame-speed predictions. As shown in the right panel of Fig. 7, the ±20% uncertainty in the CH_3 mole fraction reduces the uncertainty of the predicted flame speeds by 50%; and a ±10% uncertainty yielded even better results. Also shown in the same figure is the result of a similar analysis using the OH profile only. Clearly, the OH profiles provided stronger constraints to the model uncertainty than the CH_3 profiles. The cause is quite obvious, in that the OH profiles contain information both in the induction-period radical chain branching process and the heat release rates after the induction period. Of course, considering all species profiles of Series 1 and 2 experiments gives the most stringent constraint on the flame-speed prediction.

The results presented above also confirm that the prior model can reconcile nearly all species profile data considered and that the two species datasets are consistent with each other within the framework of the prior model used, except for the very early stage of the CH_3 profile. As shown in the left panel of Fig. 9, consideration of both sets of species data in the least-squares minimization scheme led to a posterior model (Model III) equally accurate and precise for prediction of the OH profile as compared to the case in which the CH_3 profiles were excluded from the minimization. In the right panel of Fig. 9, we show the Series 1*i* OH prediction for Model IV, which was constrained by the global combustion properties, including the flame speed and ignition delay. It can be seen that the scatter in the predicted OH concentration is marginally smaller than that predicted with the prior model (*cf*, Fig. 4), but the nominal concentrations predicted for OH is significantly lower than the experiments in the post-induction period. Hence, as one may expect, while detailed species time histories present notable improvements in the precision of model predictions against global combustion properties, these global properties provide little constraints on the detailed evolution of key species concentrations during *n*-heptane oxidation.

Combining the multispecies time-history data with global combustion properties led to a posterior model fully constrained by the current knowledge considered, or Model V. As shown in Fig. 6d, the precision of the predicted flame speed is now either almost

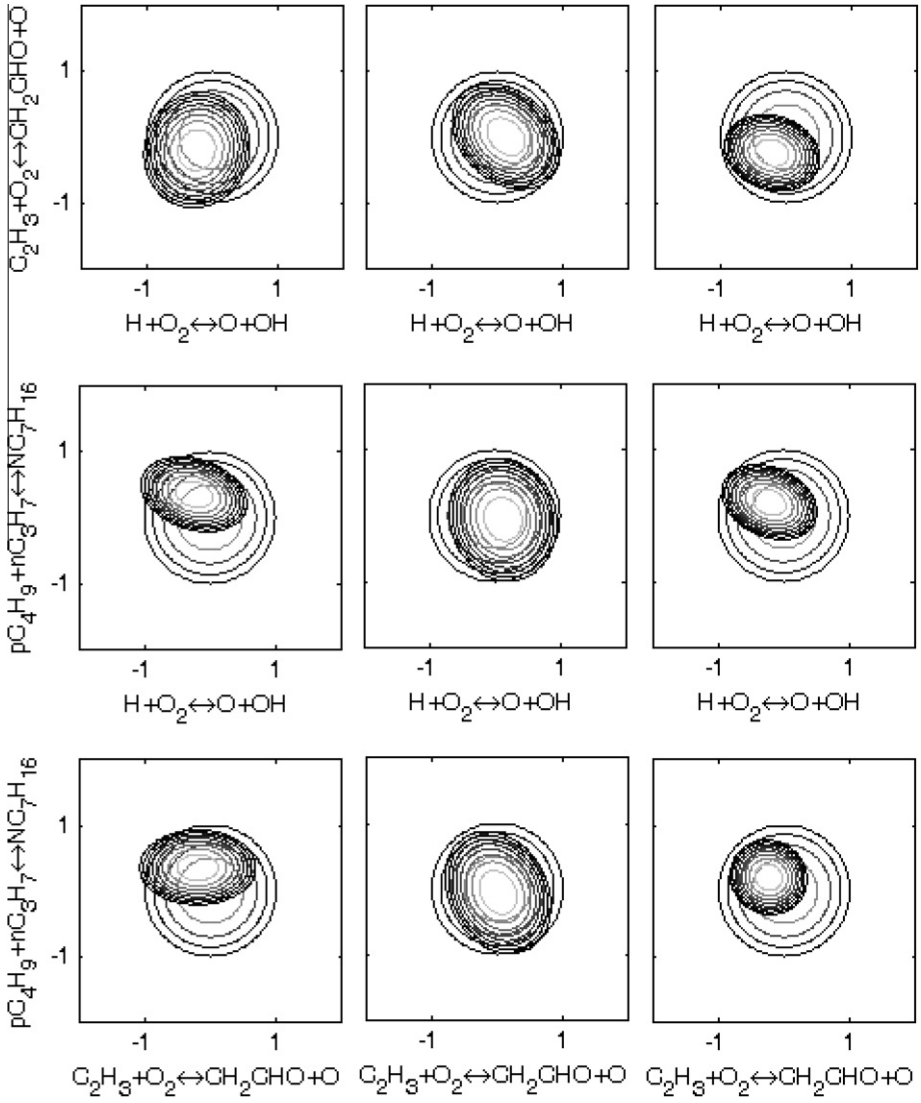

Fig. 13. Contour plots of probability density functions of the individual rate parameters. Circles correspond to the prior model. Left panels: Models III; center panels: IV; right panels: Model V.

the same as or better than the experimental uncertainties. The results illustrate that a combined consideration of the detailed, multispecies profiles in conjunction with the global combustion properties is necessary for deriving a highly accurate and precise model. Hence, highly-accurate measurements of global combustion properties remain to be valuable in the development of fundamental reaction mechanisms.

Figure 10 shows comparison of model accuracy and precision of ignition delay times of a stoichiometric *n*-heptane–oxygen–argon mixture (Series 3*ia*, p_5 = 1 atm). The top panel corresponds to the prior model and the bottom panel represents Model V. Figure 11 presents the ignition delay times for Series 3*ib*, 3*ii*, and 3*iii*. As seen, Model V gives significantly improved accuracy and precision for the experimental data over the entire temperature range. Interestingly, Model V is unable to reconcile with the experimental data at the elevated pressure of 2 atm (ϕ = 1) and under the fuel rich condition of ϕ = 2 (p_5 = 1 atm). In particular, both sets of the data show a pronounced curvature for $T_5 > \sim$1500 K; and the model predictions fall out of the uncertainty band of the data (defined by the two solid lines) and show notably shorter ignition delay times than the experiment. These results suggest a certain physical deficiency of the model above 1500 K, which cannot be accounted for with the parameter uncertainty in the prior model. While the chemistry details responsible for the discrepancy will be discussed in a future work, it is noted that the above results in fact highlight the usefulness of MUM-PCE, in that the analysis using this method can isolate the model uncertainties due to the existence of physical deficiency in a reaction model from those due to imprecise knowledge in the rate parameters.

Lastly, we discuss the different aspect of model constraints imposed by the multispecies time-history data and by the global combustion properties. Figure 12 presents the covariance matrices Σ (presented as $K_{ij} = \sqrt{|\Sigma_{ij}|}$) computed for Model II (top panel) and Model IV (bottom panel). Though there is a tremendous, joint constraining effect from both types of data, the constraint from the species profiles is predominantly imposed on reactions of radical chain branching and those involving CH_x radicals, propene, and the parent-fuel breakup. A similar effect can be seen in the reaction rate parameters for Model II in Table S3, where these same reaction rates are those that must be modified by the largest factors in order to reproduce the species profile measurements. Flame speeds and ignition delay appear to constrain more strongly the heat release and chain branching reactions. Figure 13 presents contour plots of the probability density functions of three individual rate constants, where the left, center and right columns represent Model III (species profiles), Model IV (global combustion properties) and Model V. As seen, the rate parameter of the initial C–C fission reaction $nC_7H_{16} \rightarrow pC_4H_9 + nC_3H_7$ is not constrained by the global properties, but it is constrained notably by the species profiles. This constraint turns out to have a large effect on the joint rate parameter uncertainty space. As the right panels show, the size of the original joint uncertainty space of the three rate parameters is reduced significantly, by as much as a factor of 4–8, when both detailed species time history and global combustion property data are used to constrain the model parameter uncertainty.

7. Conclusion

A set of data containing the recently reported multispecies time histories during *n*-heptane oxidation behind reflected shock waves were utilized along with global combustion properties (flame speed and ignition delay) to analyze and improve the accuracy and precision of a modified JetSurF mechanism. The results may be summarized as follows:

(1) For *n*-heptane combustion the kinetic uncertainty in JetSurF is substantially larger than the uncertainty in the experimental dataset considered. In particular, the reaction model is shown to be accurate in predicting the experiments, but the precision of the model is rather poor.
(2) The high-precision species measurements were shown to provide a strong constraint on the model predictions of species profiles, as well as global combustion properties. In some cases, the prediction precision was improved by as much as a factor of 3. Strong constraints were imposed on the joint uncertainty space of the rate parameters of radical chain branching/heat release reactions, as well as the parent-fuel breakup, CH_x and propene reactions. On the other hand, global combustion properties (laminar flame speeds and ignition delay times) were shown to provide constraints more on reactions involved in heat release.
(3) Lastly, while the high-precision species measurements in shock tubes are proven to be critical toward future kinetic model development, global flame property measurements are still necessary to achieve highly accurate and precise predictions for fuel combustion.

Acknowledgments

The work was sponsored in part by the US Air Force Office of Scientific Research AFOSR (Grant Nos. FA9550-07-1-0168 and FA9550-08-1-0040) under the technical supervision of Dr. Julian M. Tishkoff and by the Combustion Energy Frontier Research Center (CEFRC), an Energy Frontier Research Center funded by the US Department of Energy, Office of Science, Office of Basic Energy Sciences under Award Number DE-SC0001198.

Appendix A. Supplementary material

Supplementary data associated with this article can be found, in the online version, at doi:10.1016/j.combustflame.2010.12.016.

References

[1] R.K. Hanson, Proc. Combust. Inst. 33 (2010) 1–40.
[2] D.F. Davidson, R.K. Hanson, Shock Waves 19 (2009) 271–283.
[3] D.F. Davidson, Z. Hong, G.L. Pilla, A. Farooq, R.D. Cook, R.K. Hanson, Combust. Flame 157 (2010) 1899–1905.
[4] D.F. Davidson, Z. Hong, G.L. Pilla, A. Farooq, R.D. Cook, R.K. Hanson, Proc. Combust. Inst. 33 (2010) 151–157.
[5] D.A. Sheen, X. You, H. Wang, T. Løvås, Proc. Combust. Inst. 32 (2009) 535–542.
[6] D.F. Davidson, M.A. Oehlschlaeger, R.K. Hanson, Proc. Combust. Inst. 31 (2007) 321–328.
[7] H.J. Curran, P. Gaffuri, W.J. Pitz, C.K. Westbrook, Combust. Flame 114 (1998) 149–177.
[8] M. Chaos, A. Kazakov, Z. Zhao, F.L. Dryer, Int. J. Chem. Kinet. 39 (2007) 399–414.
[9] B. Sirjean, E. Dames, D.A. Sheen, X. You, C.J. Sung, A.T. Holley, F.N. Egolfopoulos, H. Wang, S.S. Vasu, D.F. Davidson, R.K. Hanson, H. Pitsch, C.T. Bowman, A. Kelley, C.K. Law, W. Tsang, N.P. Cernansky, D. Miller, A. Violi, R.P. Lindstedt, A high-temperature chemical kinetic model of *n*-alkane oxidation, JetSurF version 1.0., 2009. <http://melchior.usc.edu/JetSurF/JetSurF1.0/Index.html>.
[10] X. You, F.N. Egolfopoulos, H. Wang, Proc. Combust. Inst. 32 (2009) 403–410.
[11] H. Wang, X. You, A.V. Joshi, S.G. Davis, A. Laskin, F.N. Egolfopoulos, C.K. Law, USC Mech Version II. High-temperature combustion reaction model of H_2/CO/C_1–C_4 compounds, 2007. <http://ignis.usc.edu/Mechanisms/USC-Mech20II/USC_Mech20II.htm>.
[12] S.G. Davis, A.V. Joshi, H. Wang, F.N. Egolfopoulos, Proc. Combust. Inst. 30 (2005) 1283–1292.
[13] S.G. Davis, C.K. Law, H. Wang, Combust. Flame 119 (1999) 375–399.
[14] S.G. Davis, C.K. Law, H. Wang, J. Phys. Chem. A 103 (1999) 5889–5899.
[15] A. Laskin, H. Wang, Chem. Phys. Lett. 303 (1999) 43–49.
[16] A. Laskin, H. Wang, C.K. Law, Int. J. Chem. Kinet. 32 (2000) 589–614.
[17] Z. Qin, V. Lissianski, H. Yang, W.C. Gardiner Jr., S.G. Davis, H. Wang, Proc. Combust. Inst. 28 (2000) 1663–1669.
[18] H. Wang, Int. J. Chem. Kinet. 33 (2001) 698–706.

[19] T. Hirasawa, C.J. Sung, A. Joshi, Z. Yang, H. Wang, C.K. Law, Proc. Combust. Inst. 29 (2003) 1427–1434.
[20] C.K. Law, C.J. Sung, H. Wang, T.F. Lu, AIAA J. 41 (2003) 1629–1646.
[21] A.V. Joshi, H. Wang, Int. J. Chem. Kinet. 38 (2006) 57–73.
[22] R. Sivaramakrishnan, A. Comandini, R.S. Tranter, K. Brezinsky, S.G. Davis, H. Wang, Proc. Combust. Inst. 31 (2007) 429–437.
[23] X.Q. You, H. Wang, E. Goos, C.J. Sung, S.J. Klippenstein, J. Phys. Chem. A 111 (2007) 4031–4042.
[24] C. Ji, E. Dames, Y.L. Wang, H. Wang, F.N. Egolfopoulos, Combust. Flame 157 (2010) 277–287.
[25] D.L. Baulch, C.J. Cobos, R.A. Cox, C. Esser, P. Frank, T. Just, J.A. Kerr, M.J. Pilling, J. Troe, R.W. Walker, J. Warnatz, J. Phys. Chem. Ref. Data 21 (1992) 411–734.
[26] Z. Hong, S.S. Vasu, D.F. Davidson, R.K. Hanson, J. Phys. Chem. A 17 (2010) 5520–5525.
[27] N.K. Srinivasan, M.C. Su, J.W. Sutherland, J.V. Michael, B. Ruscic, J. Phys. Chem. A 110 (2006) 6602–6607.
[28] H. Hippler, H. Neunaber, J. Troe, J. Chem. Phys. 103 (1995) 3510–3516.
[29] C. Kappel, K. Luther, J. Troe, Phys. Chem. Chem. Phys. 4 (2002) 4392–4398.
[30] D.L. Baulch, C.T. Bowman, C.J. Cobos, R.A. Cox, T. Just, J.A. Kerr, M.J. Pilling, D. Stocker, J. Troe, W. Tsang, R.W. Walker, J. Warnatz, J. Phys. Chem. Ref. Data 34 (2005) 757–1397.
[31] J.M. Smith, J.M. Simmie, H.J. Curran, Int. J. Chem. Kinet. 37 (2005) 728–736.
[32] D.F. Davidson, S.C. Ranganath, K.-Y. Lam, M. Liaw, Z. Hong, R.K. Hanson, J. Propul. Power 26 (2010) 280–287.
[33] J. Warnatz, Proc. Combust. Inst. 24 (1992) 553–579.
[34] T. Turanyi, L. Zalotai, S. Dobe, T. Berces, Phys. Chem. Chem. Phys. 4 (2002) 2568–2578.
[35] J. Zádor, I.G. Zsély, T. Turányi, Reliab. Eng. Syst. Safety 91 (2006) 1232–1240.
[36] J. Zador, I.G. Zsely, T. Turanyi, M. Ratto, S. Tarantola, A. Saltelli, J. Phys. Chem. A 109 (2005) 9795–9807.
[37] I.G. Zsely, J. Zador, T. Turanyi, Proc. Combust. Inst. 30 (2005) 1273–1281.
[38] I.G. Zsély, J. Zádor, T. Turányi, Int. J. Chem. Kinet. 40 (2008) 754–768.
[39] K.J. Hughes, T. Turanyi, A.R. Clague, M.J. Pilling, Int. J. Chem. Kinet. 33 (2001) 513–538.
[40] T. Ziehn, A.S. Tomlin, Int. J. Chem. Kinet. 40 (2008) 742–753.
[41] J.L. Beck, L.S. Katafygiotis, J. Eng. Mech. 124 (1998) 455–461.
[42] L.S. Katafygiotis, J.L. Beck, J. Eng. Mech. 124 (1998) 463–467.
[43] A.A. Taflanidis, J.L. Beck, J. Eng. Mech. 1 (2010) 145.
[44] J.L. Beck, S.-K. Au, J. Eng. Mech. 128 (2002) 380–391.
[45] R. Feeley, M. Frenklach, M. Onsum, T. Russi, A. Arkin, A. Packard, J. Phys. Chem. A 110 (2006) 6803–6813.
[46] R. Feeley, P. Seiler, A. Packard, M. Frenklach, J. Phys. Chem. A 108 (2004) 9573–9583.
[47] M. Frenklach, A. Packard, P. Seiler, R. Feeley, Int. J. Chem. Kinet. 36 (2004) 57–66.
[48] D.A. Sheen, H. Wang, Combust. Theory Model., submitted for publication.
[49] M. Frenklach, Combust. Flame 58 (1984) 69–72.
[50] M. Frenklach, H. Wang, M.J. Rabinowitz, Prog. Energy Combust. Sci. 18 (1992) 47–73.
[51] N. Weiner, Am. J. Math. 60 (1938) 897–936.
[52] D. Xiu, G.E. Karniadakis, SIAM J. Sci. Comput. 24 (2002) 619–644.
[53] M.T.R.H.N. Najm, R.G. Ghanem, O.M. Kino, Combust. Flame 132 (2003) 545–555.
[54] M.T. Reagan, H.N. Najm, B.J. Debusschere, O.P.L. Maitre, O.M. Kino, R.G. Ghanem, Combust. Theory Model. 8 (2004) 607–632.
[55] M.T. Reagan, H.N. Najm, P.P. Pépey, O.M. Kino, R.G. Ghanem, Int. J. Chem. Kinet. 37 (2005) 368–382.
[56] S.G. Davis, A.B. Mhadeshwar, D.G. Vlachos, H. Wang, Int. J. Chem. Kinet. 36 (2004) 94–106.
[57] G.E.P. Box, R.D. Meyer, J. Res. Natl. Bur. Stand. 90 (1985) 495–500.
[58] R.J. Kee, F.M. Rupley, J.A. Miller, CHEMKIN-II: A FORTRAN Chemical Kinetics Package for the Analysis of Gas-phase Chemical Kinetics, SAND89-8009, Sandia National Laboratories, Albuquerque, NM, 1989.
[59] R.J. Kee, J.F. Grcar, M.D. Smooke, J.A. Miller, A FORTRAN Program for Modeling Steady Laminar One-dimensional Premixed Flames, SAND85-8240, Sandia National Laboratories, Albuquerque, NM, 1986.
[60] P. Middha, H. Wang, Combust. Theory Model. 9 (2005) 353–363.
[61] Y. Dong, A.T. Holley, M.G. Andac, F.N. Egolfopoulos, S.G. Davis, P. Middha, H. Wang, Combust. Flame 142 (2005) 374–387.
[62] G.E.P. Box, G.C. Tiao, Bayesian Inference in Statistical Analysis, Wiley, New York, NY, 1973.